Geophys. J. Int. (2006) **171,** 435–450 doi: 10.1111/j.1365-246X.2006.03498.x

Numerical comparison of different convergent plate contacts: subduction channel and subduction fault

Roberta De Franco, Rob Govers and Rinus Wortel

Faculty of Geosciences, Utrecht University, Utrecht, The Netherlands. E-mail: defranco@geo.uu.nl

Accepted 2007 May 14. Received 2007 February 1; in original form 2006 October 30

SUMMARY

At convergent plate boundaries, the properties of the actual plate contact are important for the overall dynamics. Convergent plate boundaries both mechanically decouple and link tectonic plates and accommodate large amounts of strain. We investigate two fundamental physical states of the subduction contact: one based on a fault and the other based on a subduction channel. Using a finite element method, we determine the specific signatures of both states of the subduction contact. We pay particular attention to the overriding plate. In a tectonic setting of converging plates, where the subducting plate is freely moving, the subduction channel reduces compression relative to the fault model. In a land-locked basin setting, where the relative motion between the far field of the plates is zero, the subduction channel model produces tensile stress regime in the overriding plate, even though the amount of slab roll-back is small. The fault model shows a stronger development of slab roll-back and a compressive stress regime in the upper plate. Based on a consistent comparison of fault and channel numerical models, we find that the nature of the plate contact is one of the controlling factors in developing or not of backarc extension. We conclude that, the type of plate contact plays a decisive role in controlling the backarc state of stress. To obtain backarc extension, roll-back is required as an underling geodynamic process, but it is not always a sufficient condition.

Key words: backarc deformation, fault, numerical modelling, plate contact, subduction, subduction channel.

Downloaded from https://academic.oup.com/gji/article/171/1/435/2126931 by guest on 21 July 2021

1 INTRODUCTION

Whereas several correlations between observed parameters in subduction zones have been established, the physical meaning of such correlations is only partially understood. In convergent plate boundaries, the properties of the actual plate contact are important for the overall dynamics. For the operation of plate tectonics a relatively low shear strength is a critical mechanical property of plate contacts (Tackley 2000). The effective friction at a subduction zone has a first order control on plate boundary topography and the plate-like motion (Zhong *et al.* 1998). In the most simple representation the plate contact is a single fault, and the friction coefficient controls the jump in fault parallel velocities across the fault, that is, the level of decoupling. Plate contacts between oceanic plates come closest to such single fault representation, but even there closer examination consistently shows that strain is distributed.

In the late seventies and early 1980s 2-D models were introduced with a weak subduction contact zone of few hundred kilometres wide (Kapitzke 1979; Schmeling & Jacoby 1981; Jacoby & Schmeling 1982). The weak zones were used to localize deformation and to mimic rheological stress weakening. The limitation of such formulation was that the deformation was distributed over the entire weak zone which conflicted with seismic observations. Shreve & Cloos (1986) proposed that the descending plate carries a layer of sediments down into a relatively thin subduction channel (0.3–5.3 km) beneath the overriding block. These sediments were proposed to act as a lubricating layer. The transmission of velocity and stress between plates was regulated by the dimension, the pressure distribution and the rheology of the channel (Shreve & Cloos 1986).

More observational support for channel of a few kilometres has been collected since. All over the world, seismic studies have shown the presence of interplate sedimentary channel-like units of about 1–8 km (Eberhart-Phillips & Martin 1999; Tsuru *et al.* 2002; Oncken *et al.* 2003; Abers 2005). More indirect evidence for a subduction channel comes from the observation of high-pressure and ultrahigh-pressure metamorphic minerals in relicts of continental crust, which document pressures in excess of 3 GPa (corresponding to a depth of about 100 km) at relatively low temperatures. The common interpretation of these observations is that the sediments were subducted and subsequently exhumed very rapidly (Smith 1984; Chopin 2001). A subduction channel was invoked to explain this process and it was quantitatively modelled by Gerya *et al.* (2002).

There are two reasons why the sediment channel cannot be a good description of all subduction zones. First, great subduction earthquakes attest to the fact that the subduction interface cannot be

© 2006 The Authors
Journal compilation © 2007 RAS

weak everywhere (Davies & Brune 1971; Kanamori 1977; Ruff & Kanamori 1983; Tichelaar & Ruff 1993). Most interplate seismicity occurs at depth range of 0–50 km (Tichelaar & Ruff 1993), meaning that at least the shallow part of the subduction zone has a finite shear strength. Second, sediment supply varies widely from site to site as indicated by accretionary wedge dimensions and erosive margin observations. This means that when the amount of sediments is small, the subduction channel becomes so thin that a more appropriate description of the plate contact is by one or several faults. Fault normal velocities and tractions are continuous, and plates are fully coupled in this direction.

On the scale of the entire lithosphere, quantitative models based on a single throughgoing subduction fault have been used to investigate how the fault properties influence the stress distribution and plate boundary forces associated with subduction (Bott *et al.* 1989; Whittaker *et al.* 1992; Giunchi *et al.* 1996). Zhong & Gurnis (1994a,b), and Zhong *et al.* (1998) pointed out that a subducting slab with a fault produces plate like behaviour, trench and fore bulge topography and principal stresses consistent with observations.

Thus, there is support for both types of contact zones. The fault and the subduction channel represent two different physical states of the subduction plate contact. A subduction zone may evolve from one state to another through a varying sediment supply. Along strike variations in the physical state of a single subduction zone are also conceivable.

Another fundamental aspect governing the response of subduction is the tectonic setting of the plates. In subduction zones, the range of tectonic settings is wide; for instance, the overriding plate can be driven towards or away from the trench or be stationary; the subducting plate can be actively driven into the subduction zone, or not. Another possibility is that collision effectively hampers further subduction. Clearly, the stress and the velocity distribution of the area are affected by these factors. Here we focus on tectonic settings where motions are driven entirely within the model domain: (1) the setting in which the overriding plate is stationary in the far field and the oceanic subducting plate is freely moving (free subduction) and (2) a land-locked basin setting where there is no net convergence between the surface plates, so that subduction must occur through roll-back (e.g. Mediterranean basin).

The aim of our study is to determine the specific signatures of both states of subduction zones, that is, a subduction fault and a subduction channel, in these tectonic settings. Through numerical modelling we evaluate overriding plate velocities, stress field in the backarc region and topography for both types. By using a single finite element program for both types of models, the results are internally consistent and, therefore, well suited for comparison.

2 NUMERICAL METHOD AND MODEL SETUP

For the purpose of this study we focus on a generic subduction zone, that is, we do not focus on any particular convergent plate boundary. In such a generalized subduction zone we choose to omit some of the geometric details that have been documented by the recent compilation by Lallemand *et al.* (2005). While important for making accurate predictions for any real subduction zone, these details do not affect the principal functioning of the subduction zone and would merely add complexity that clouds our understanding of the physical process. One major simplification we make for this very same reason is that the subduction zone is well represented by a 2-D cross-section (Fig. 1).

The long-term mechanics of the lithosphere and upper mantle is governed by the momentum equation. We solve this partial differential equation for instantaneous velocities and stresses using the plain strain approximation. We use the G-TECTON finite element code (Govers & Wortel 1993), which was developed from TECTON version 1.3 (Melosh & Raefsky 1983), to solve the momentum equation. Constitutive laws in the model represent elastic, viscous and plastic deformation.

Viscosity is taken to be strongly temperature dependent, in accordance with rock mechanical experiments in both the power law and diffusion creep regime (e.g. Kohlsteldt & Zimmerman 1996). Density also depends on temperature and we adopt a linear equation of state in our model. These dependences make it necessary to also solve for model temperature.

The initial temperature field is computed with a new finite element solver in G-TECTON for the steady state diffusion-advection equation. This solver is based on a streamline upwind Petrov-Galerkin (SUPG) formulation (see Appendix A). A unique feature of our implementation is that we facilitate discontinuities in the velocity field (at faults) via a split node technique. The temperature solutions were verified to be identical to those resulting from integrating the time-dependent conduction equation for a long time (finite difference code of van de Zedde & Wortel (2001)). As the mechanical models of this paper focus on short timescales, relative to a thermal diffusion timescale, we ignore the temporal evolution of conduction. We do account for advective heat transport through the Lagrangian motion of the numerical grid.

We assume the surface oceanic lithosphere has an age of 33 Myr at the right-hand model boundary. Here the initial geotherm is defined using a half-space cooling model. Using a convergence velocity of 4 cm yr^{-1}, which in our models corresponds to the spreading rate of the oceanic lithosphere, the oceanic age at the trench is of 70 Myr. Temperatures in the continental overriding plate are based

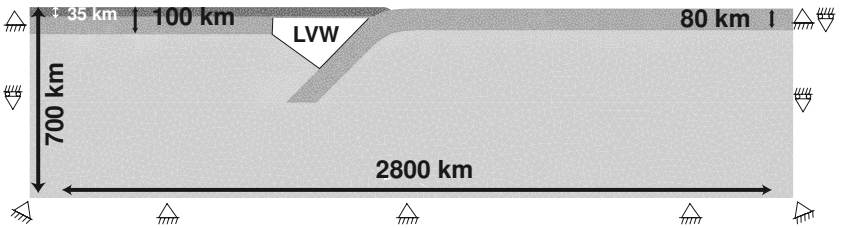


Figure 1. Model setup. On the left the continental plate with the continental crust on top, on the right the oceanic plate. Boundary conditions: on the bottom no displacement; on the left: the lithosphere is locked, in the mantle horizontal displacement is allowed; on the right: the lithosphere is locked, in the mantle horizontal displacement is allowed.

Downloaded from https://academic.oup.com/gji/article/171/1/435/2126031 by guest on 21 July 2021

Table 1. Thermal and mechanical model parameters.

Thermal properties	k conductivity	H heat production	C_p specific heat	
Continental crust	3.2 W m^{-1} K^{-1}	6.81×10^{-7} W m^{-3}	1×10^3 J kg^{-1} K^{-1}	
Lithosphere	3.2 W m^{-1} K^{-1}	0	1×10^3 J kg^{-1} K^{-1}	
Mantle	5.1 W m^{-1} K^{-1}	0	1×10^3 J kg^{-1} K^{-1}	
Elastic properties	E Young's modulus	ν Poisson's modulus		
Continental crust	5×10^{10} Pa	0.3		
Lithosphere	5×10^{10} Pa	0.3		
Mantle	1×10^{11} Pa	0.3		
Creep properties	A pre-exponent	Q activation energy	V activation volume	n stress power
Continental crust	3.3×10^{-21} Pa^{-n} s^{-1}	163 kJ mole^{-1}	17×10^{-6} m^3 mole^{-1}	3
Mantle $<$ 350 km	1.317×10^{-14} Pa^{-n} s^{-1}	485 kJ mole^{-1}	25×10^{-6} m^3 mole^{-1}	3
Mantle $>$ 350 km	1.54×10^{-11} Pa^{-n} s^{-1}	270 kJ mole^{-1}	6×10^{-6} m^3 mole^{-1}	1

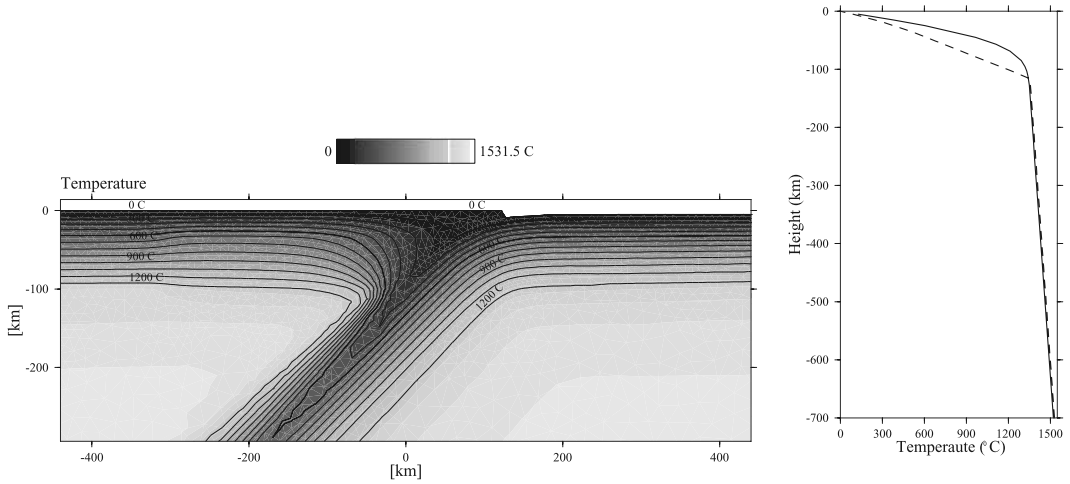


Figure 2. Left-hand side: Total temperature distribution. Right-hand side: geotherm at the sides of the model domain. Solid curve: temperature boundary condition at the right-hand side of the model; dashed curve: temperature boundary condition at the left-hand side of the model.

on a representative steady state geotherm with a surface heat flow of 65 mW m^{-2} (Table 1). We use a adiabatic gradient of 0.3 K per km. Temperature boundary conditions at the top and bottom of the model domain are 0 and 1531 °C. The initial temperature field is displayed in Fig. 2 (left-hand side). Temperatures at the right- and left-hand side of the model correspond to the two geotherms plotted in Fig. 2 (right-hand side).

The velocity field to compute the initial temperatures has a uniform velocity of 4 cm yr^{-1} for both the surface oceanic plate and the slab. Velocity directions are everywhere parallel to the local mid-plane orientation to avoid a deviations from incompressible flow. In the temperature calculations, the velocity of the continental lithosphere is uniformly set to zero. The velocity field in the arc corner is calculated using an analytical corner flow solution, which depends on the subduction velocity and on the angle of subduction.

Our model domain is 700 km deep and 2800 km wide (Fig. 1). The subducting oceanic plate is on the right, the overriding plate on the left. The shape of the curved slab is defined by an error function (Govers & Wortel 2005); we adopt a radius of curvature R of 1.6 L (L being the thickness of the oceanic lithosphere, that is, 80 km) and final dip angle θ of 45°. The slab initially extends to 350 km depth. The overriding plate is 100 km thick, and has a crustal thickness of 35 km.

The rheology of our model is elastic, viscous, or plastic and depends on composition, temperature, pressure and stress (Table 1). The viscosity η of steady state flow can be written as:

$$\eta = \frac{1}{2A} \exp\Big(\frac{Q + pV}{RT}\Big)\sigma_E^{-(n-1)}, \quad (1)$$

where A is the pre-exponent, Q the activation energy, p pressure, V activation volume, R universal gas constant, T temperature, and $\sigma_E \equiv \sqrt{\frac{1}{2}\sigma'_{ij}\sigma'_{ij}}$ the effective stress.

Model viscosities follow from either steady state dislocation creep or diffusion creep. We choose model parameters following Karato & Wu (1993) for the mantle (the parameters are chosen to be intermediate between their wet and dry values (van Thienen *et al.* 2003) and Freed & Burgmann (2004) for the continental crust (see Table 1)). If $n > 1$, the viscosity is stress dependent as a result of dislocation creep. Steady state diffusion creep results in a viscosity which is independent of stress ($n = 1$) and depends on grain size. This grain size dependence is not apparent in eq. (1) because we assume a uniform grain size of 1 mm and grain size exponent of 2.5 to correct the pre-exponential term. Dislocation creep is assumed to prevail to a depth of 350 km, and diffusion creep in the transition zone (Karato & Wu 1993).

We use a low viscosity mantle wedge (LVW) in order to reduce the down-warping of the overriding plate in the arc/backarc region

Downloaded from https://academic.oup.com/gji/article/171/1/435/2126031 by guest on 21 July 2021

(Billen & Gurnis 2001). The mantle wedge is the region of the mantle lithosphere and asthenosphere above the subducting slab (Fig. 1). In our model, we assume a uniform viscosity of 1×10^{19} Pa s in the mantle wedge.

We use an isotropic Von Mises criterion to limit deviatoric stresses in accordance with Byerlee's law (Byerlee 1978) with hydrostatic fluid pressure and horizontal compression. Yield strength increases linearly with pressure and it is expressed by the equation:

$$Y = \frac{\sqrt{3}}{2}(R-1)(1-\lambda)p, \tag{2}$$

where Y is the yield strength, R depends on the friction coefficient, λ is the pore fluid pressure, p is the pressure. Viscoplastic flow results in permanent deformation in case deviatoric stresses exceed the yield strength. The resulting relaxation brings stresses back to the yield strength level.

We adopt two descriptions for the active plate contact: a subduction fault and a subduction channel, with the following characteristics:

(1) A deformable subduction fault is described via updated slippery nodes, in which the fault slip is locally kept parallel to the fault (Buiter *et al.* 2001). In most models, fault friction is negligible. We name this class of models fault no friction (FNF). We will also present models with a frictional fault (FF).

(2) A subduction channel separates the subducting and the overriding plate. The channel width is assumed to be approximately 6 km (Shreve & Cloos 1986; Beaumont & Ellis 1999). Channel viscosity is taken to be Newtonian, ranging from 7×10^{17} Pa s in our 'low viscosity channel' (LVC) models (England & Holland 1979; Shreve & Cloos 1986) to 10^{21} Pa s in the 'high viscosity channel' (HVC) models (Renner *et al.* 2001; Gerya *et al.* 2002; Stockhert 2002).

Following Govers & Wortel (2005), we separate model densities into a 1-D reference density profile and the remaining density anomalies. Reference densities are used to initialize hydrostatic pressures and which initially do not contribute to the forcing. The remaining density anomalies (i.e. slab pull forces) are used to drive model deformation and are instantaneously applied at the beginning of the model calculation. The initial bending stresses are not included since we assumed a pre-existing subducted slab geometry. The influence of the ridge push is excluded in order to isolate the subduction effect (Bott *et al.* 1989). In general we do not apply velocities as a forcing, except for one experiment in which we impose a velocity boundary condition of 7 cm yr^{-1} to drive the slab.

We concentrate first on models where the subducting plate is free to move in a horizontal direction. Then we study models for a landlocked basin setting (Le Pichon 1982), an example of which is the Mediterranean; a very small relative motion between continents that surround an oceanic basin has as a consequence that basin-internal subduction needs to be accompanied by backarc extension. Our boundary conditions on the lithosphere thus do not allow relative motion between the far field plates.

Our focus on the subduction zone has the consequence that we choose to ignore convective motions beneath the lithosphere which are not driven by the sinking slab or plate motions. We assume that such convection would cause similar imprints on both the subduction fault model and the subduction channel model. For comparing the two types of subduction zones, we thus consider plate-excited mantle flow only. This has one immediate consequence for the boundary conditions acting on the sublithospheric part of side boundaries: these boundaries are far enough from the central down-welling region to affect the horizontal in and outflow only beneath the lithosphere. Because viscous flow is incompressible in our formulation, this constraint has the additional consequence of requiring continuity of horizontal flow beyond our model domain. Consistent with Mitrovica & Forte (1997), we assume a significantly higher viscosity in the lower mantle beneath the lower domain boundary; in our model this is represented by no slip boundary conditions.

3 RESULTS

3.1 Free subduction

In this setup the upper plate on the left-hand side is locked via a boundary condition and the subducting plate is free to move horizontally. Fig. 3(a) shows the velocity distribution for the frictionless subduction FNF after 250 Kyr (representing about 3100 asthenospheric Maxwell times). This time was chosen on the basis of longer running preliminary experiments which showed that model spin-up signatures had vanished and that the velocity field had reached steady state.

Slab pull forces drive a primarily vertical down-welling close to the slab. Eddies are created at the two end sides of the slab. In the oceanic lithosphere, motions are mostly horizontally directed towards the plate contact region. Horizontal return flow dominates in the deeper mantle beneath the slab. Velocity patterns of the different subduction zone models are very similar in most of our model domain, except near the plate contact zone where there are important differences. Therefore, we will subsequently zoom in on this region.

3.1.1 Frictionless fault subduction zone model (FNF)

Fig. 3(b) is a blow up of the subduction region of Fig. 3(a). The subduction fault is defined along the plate interface from the trench to a depth of 100 km. Velocities are oriented towards the trench in the surface oceanic plate, and the magnitude is about 3 cm yr^{-1}. The overriding plate moves in the same direction as the subducting plate and the velocities are small, ranging from 0 and 3 mm yr^{-1}. In the slab velocities have a slab perpendicular component. Slab sinking induces higher velocities in the wedge than in the oceanic plate.

In Fig. 4(a), the solid line displays the horizontal velocity of the free surface for the entire model domain. For description purposes, the overriding plate is divided into region A, from the trench to the vertically projected tip of the slab, and region B beyond this (see Fig. 4). The trench is visible as a step velocity change at horizontal coordinate 100 km. The solid curve in Fig. 4(b) shows the total vertical displacement of the free surface. The trench is the deepest point of the curve (2 km). A 1–1.2 km depression has developed on the overriding plate in region A. Dynamic uplift of the outer bulge in the oceanic plate is approximately 500 m.

Fig. 5(a) shows principal stresses directions as arrows and effective stress as grey contours. In the overriding plate, close to plate contact, the stresses are small. Further to the left the stresses are horizontally compressive. Horizontal tensile stresses dominate the shallow surface oceanic plate. Zero friction at the plate contact can be seen as principal stresses oriented perpendicular to the interface. Stresses are negligible along the shallowest portion of the plate contact and slightly compressive at the interface with the deepest portion of the overriding crust. Significant fault normal stress develops in

Downloaded from https://academic.oup.com/gji/article/171/1/435/2126031 by guest on 21 July 2021

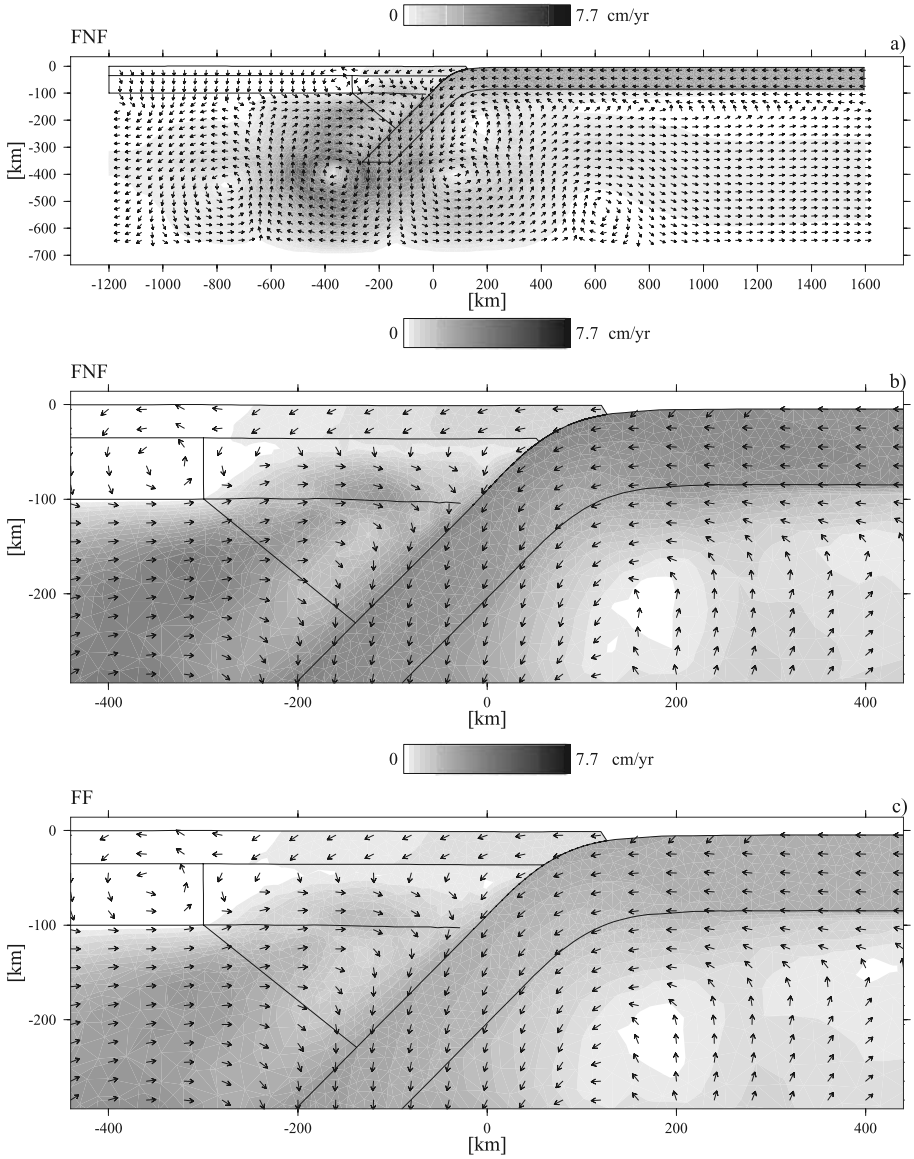


Figure 3. Steady state velocity field for free subduction boundary conditions. (a) Frictionless fault model (FNF) total view of the model domain, (b) FNF enlarged from (a), (c) Fault model with friction (FF). Note that arrows indicate directions only; arrows are not scaled by velocity magnitude. Velocity magnitude is indicated by the grey scale contours. The solid lines outline the overriding, subducting plate and the LVW. Steady state velocity filed for free subduction boundary conditions. (d) Low viscosity channel model (LVC) $\eta = 7 \times 10^{17}$ enlarged from Fig. 3(a). (e) High viscosity channel model (HVC) $\eta = 10^{20}$. Note that arrows indicate directions only; arrows are not scaled by velocity magnitude. Velocity magnitude is indicated by the grey scale contours. The solid lines outline the overriding, subducting plate and the LVW.

the slab near the downward tip of the subduction fault. Stresses within the slab do not show the typical signature of elastic bending, that is, tensile slab parallel stresses in the most shallow part and compressive stresses deeper down. Such stresses do not develop in our setup where we assumed a pre-existing subduction geometry. Our model stresses should be considered as changes due to subduction zone dynamics with respect to these typical initial flexure stresses. In the slab below 40 km depth, the compressive stresses are oriented approximately perpendicular to the slab. Stresses are low in the low-viscosity mantle wedge and beneath the oceanic surface plate.

The solid curve in Fig. 6 shows the horizontal stress of the free surface for the entire model domain. Tensile stresses dominate in the overriding plate close to the fault, and in the far field on the left-hand side (region B). A strong compression of about 150 MPa develops in region A.

3.1.2 Frictional fault subduction zone model (FF)

In our next model, we impose a uniform frictional stress of 20 MPa along the fault. The increased coupling results in a reduction of the relative velocity across the subduction zone to 2 cm yr^{-1} (Fig. 3c). The region close to the plate contact subsides more strongly and region A subsides less (grey doted line) than in FNF model (Fig. 4b). Relative to the FNF model, velocities in the mantle wedge are reduced. The main difference in the stress field is at the plate contact where compression develops, while the compressive stress in region A decreases (Figs 5b and 6).

© 2006 The Authors, *GJI*, **171,** 435–450
Journal compilation © 2007 RAS

Downloaded from https://academic.oup.com/gji/article/171/1/435/2126031 by guest on 21 July 2021

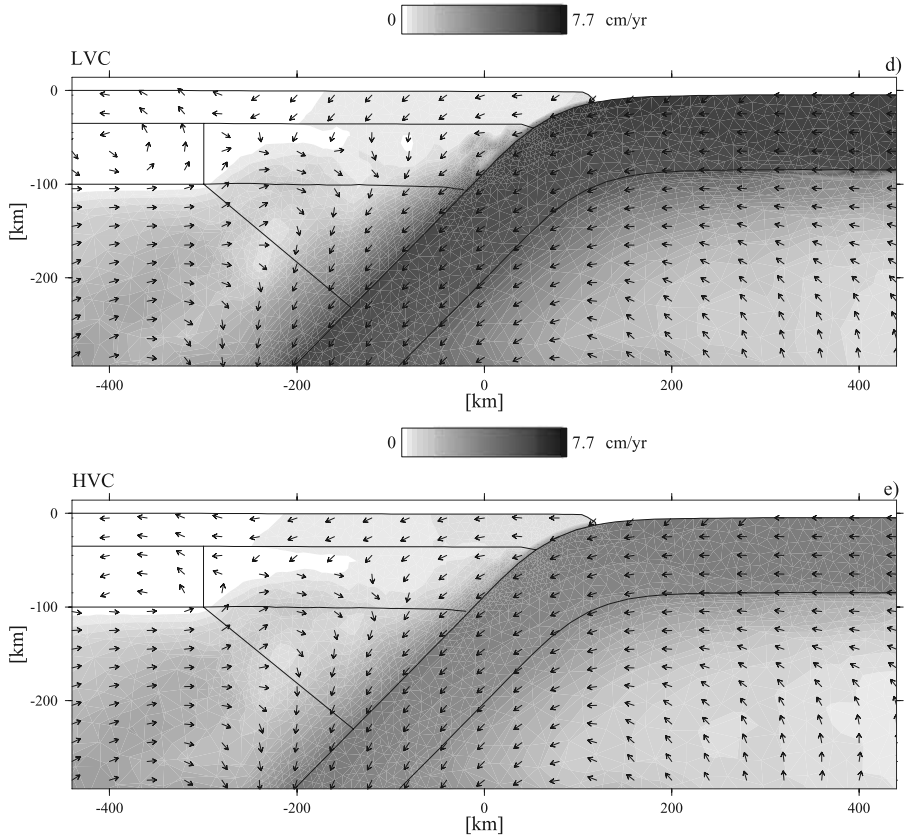


Figure 3 – *continued*

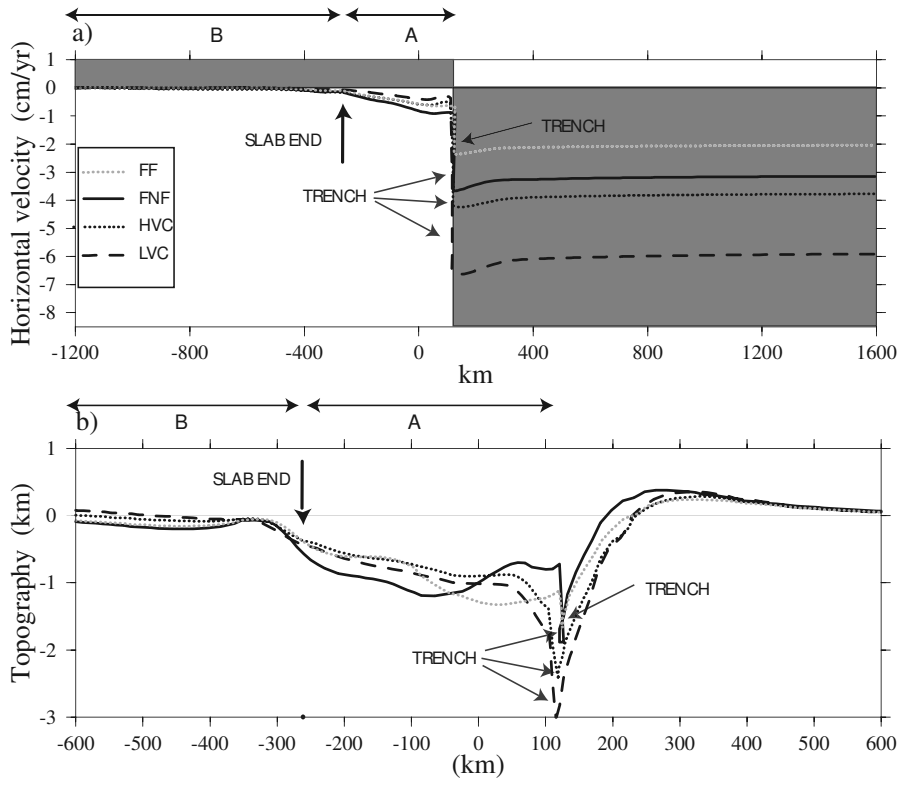


Figure 4. Surface expression for models with free subduction boundary conditions. a) Horizontal velocity at the surface of the model for the entire domain: solid curve represents frictionless fault model (FNF), grey dotted curve fault model with friction (FF), black dashed curve low viscosity channel (LVC) model $\eta = 7 \times 10^{17}$, black dotted curve high viscosity channel (HVC) model $\eta = 10^{20}$. Velocities in the grey area are directed towards the trench. b) Total vertical displacement of the surface of the model. The vertical black arrow indicates the vertically projected tip of the slab. The overriding plate is divided into region A and region B.

Downloaded from https://academic.oup.com/gji/article/171/1/435/2126031 by guest on 21 July 2021

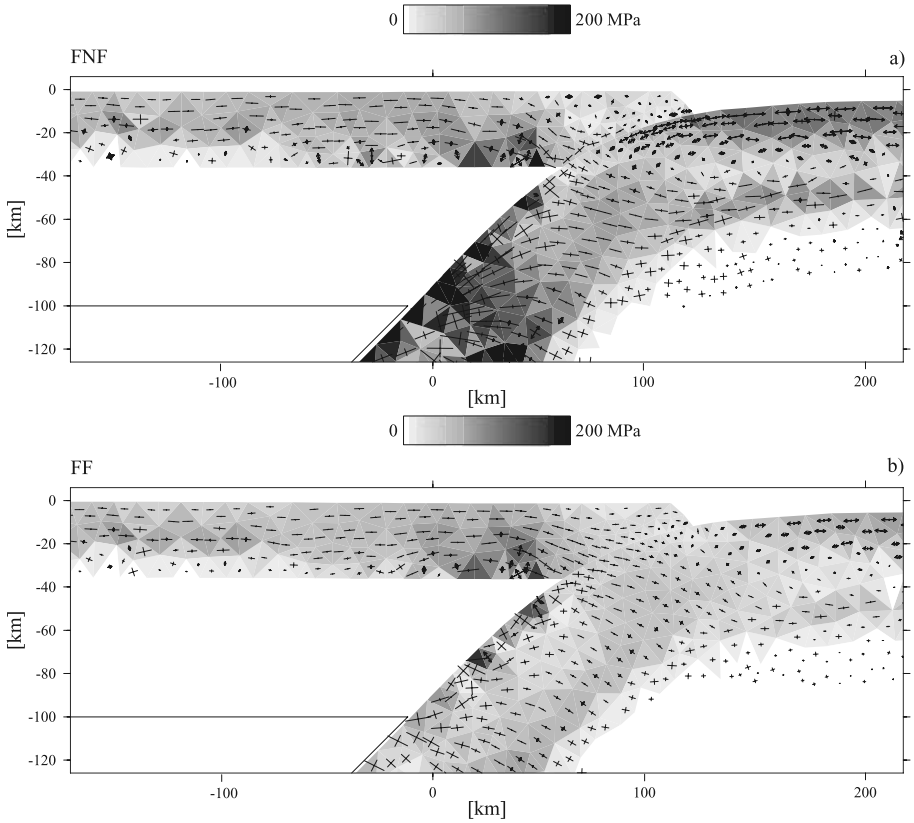


Figure 5. Effective stress magnitude and principal deviatoric stresses for models with free subduction boundary conditions. Tensile stresses are indicated by arrows, compressive stresses by lines. (a) Frictionless fault model (FNF). (b) Fault model with friction applied at the fault (FF). The black solid line indicates the initial position of the slab. Effective stress magnitude and principal deviatoric stresses for models with free subduction boundary conditions. Tensile stresses are indicated by arrows, compressive stresses by lines. (c) Low viscosity channel model (LVC) $\eta = 7 \times 10^{17}$. (d) High viscosity channel model (HVC) $\eta = 10^{20}$. The black solid line indicates the initial position of the slab.

3.1.3 Low viscosity subduction channel model (LVC)

In this model we represent the plate contact of the subduction zone by a LVC ($\eta = 7 \times 10^{17}$ Pa s). The subduction channel is defined along the plate interface from the trench to a depth of 100 km. The convergence velocity is about 7 cm yr^{-1}, which is approximately 3 cm yr^{-1} higher than in the FNF (Fig. 3d) and Fig. (4a). Velocities in the slab are uniformly plate parallel thus showing a plate like behaviour. The velocity in the overriding plate is almost uniformly zero except in the area from the trench to the projected tip of the slab (region A) where the velocity, directed to the left, implies that the trench advances with a velocity of 0.1 mm yr^{-1}. Vertical deformation is mostly less than for the FNF model except in part of region A close to the plate contact. The trench has deepened to more than 4 km, and is wider. The fore-bulge is less pronounced than in the FNF model. High velocities are excited in the asthenosphere below the overriding plate. The flow excited in the wedge below the overriding plate is lower than in the FNF model and the subducting plate moves faster than the mantle. Return flow velocities in the asthenosphere under the surface oceanic plate are lower than those in the oceanic plate itself.

In the overriding plate stresses are generally lower than in the FNF, with tension in the region close to the plate contact (see Fig. 5c) and a weaker horizontal compression in region A (Fig. 6, dashed curve). Tensile stress prevails in the upper plate far field region B (Fig. 6). Compressive stresses in region A are reduced by two orders of magnitude with respect to the FNF model. Horizontal tensile stresses dominate in the surface oceanic plate. The most shallow part of the subduction channel is visible as a zero stress layer between the oceanic slab and the continental crust. Deeper within the slab slab-parallel compression dominates. In Fig. 6 horizontal stresses are displayed with the dashed curve.

3.1.4 High viscosity subduction channel model (HVC)

The Newtonian viscosity of the subduction channel in this model is 1×10^{20} Pa s. The overall response of this model is similar to the LVC model, but there are some differences. The velocity of the subducting plate is reduced to about 4 cm yr^{-1} in Fig. 4(a). The vertical displacement is reduced as well relative to the LVC in Fig. 4(b). The trench depth is about 2 km.

The most substantial change occurs in the horizontal stress in the overriding plate (Figs 5d and 6, region A), which is more compressive. Still, however, stress levels are low compared to the FNF and the FF models.

3.2 Land-locked basin subduction

Next we present models with land-locked basin boundary conditions, that is, where the relative motion between the left and right lithospheric boundaries of the models is zero. Velocity and stress patterns of this models are very similar to the free subduction models in most of our model domain, the main differences are visible at the surface. Therefore, we will subsequently only show the surface

Downloaded from https://academic.oup.com/gji/article/171/1/435/2126031 by guest on 21 July 2021

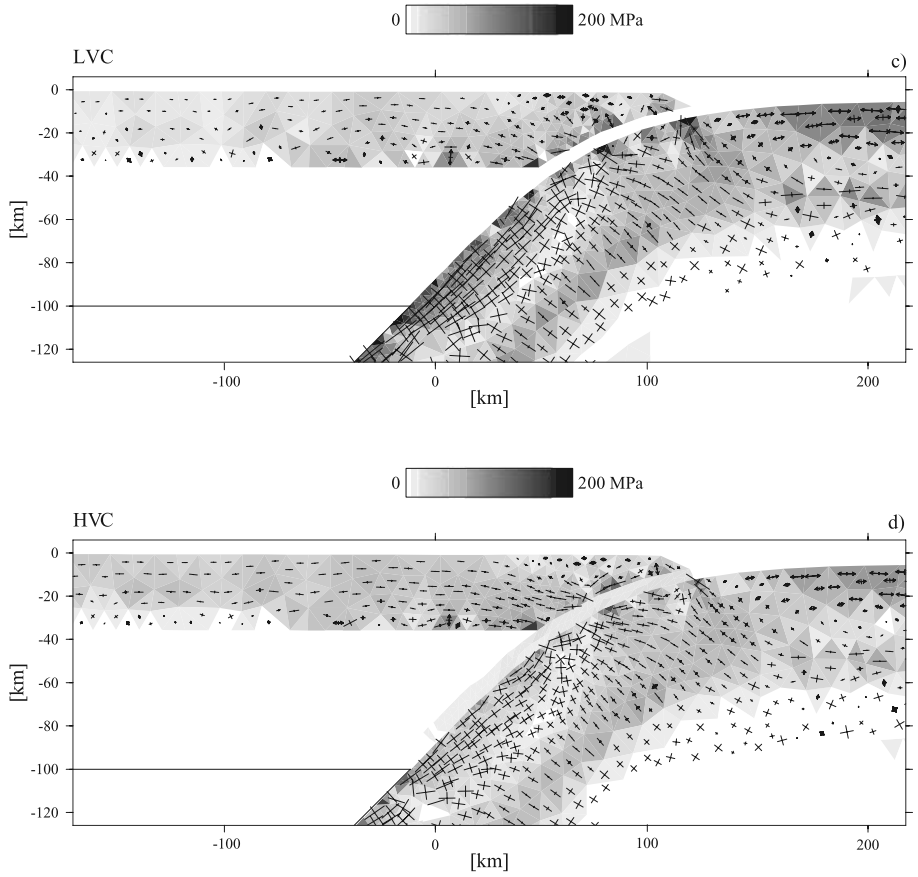


Figure 5 – *continued*

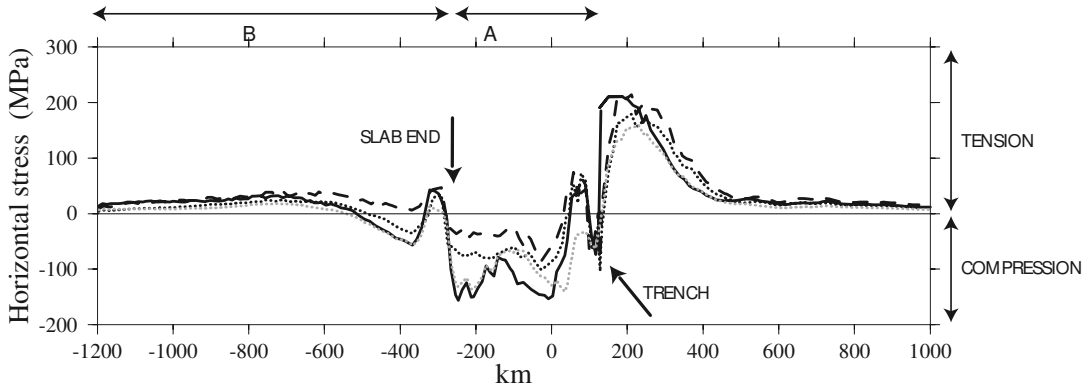


Figure 6. Horizontal stress at the free surface of free subduction the models for the entire domain. Compression is negative. Solid line represents frictionless fault model (FNF), grey dotted line fault model with friction (FF), black dashed line low viscosity model (LVC), black dotted line high viscosity model (HVC). The arrows indicate the vertical surface projection of the slab end and of the plate contact location. The overriding plate is divided into region A and region B.

expression of horizontal velocity, topography and horizontal stress in Figs 7 and 8 (more extensive results of these models are presented in the online Supplementary Material section).

3.2.1 Frictionless fault subduction zone model (FNF)

As in the previous models the subduction fault is defined along the plate interface from the trench to a depth of 100 km. The solid line in Fig. 7(a) displays the horizontal velocity of the free surface for the entire model domain. The trench is visible as a step change at horizontal coordinate 100 km. The velocity of the oceanic plate increases linearly towards the trench. The solid curve in Fig. 7(b) shows the total vertical displacement of the free surface. The trench is the deepest point of the curve (2.1 km). A 1 km deep depression has developed on the overriding plate region A. Dynamic uplift of the outer bulge on the oceanic plate is approximately 300 m.

In Fig. 8, the black line displays the horizontal stress at the free surface for the entire domain. The tensional stresses in the subducting plate (right-hand side) are higher than in the previous model (free subduction FNF model). Compression affects region A of the upper plate, but the magnitude of compression is reduced to about half of the value characterizing the free subduction FNF model, with a value of about 50 MPa.

Downloaded from https://academic.oup.com/gji/article/171/1/435/2126031 by guest on 21 July 2021

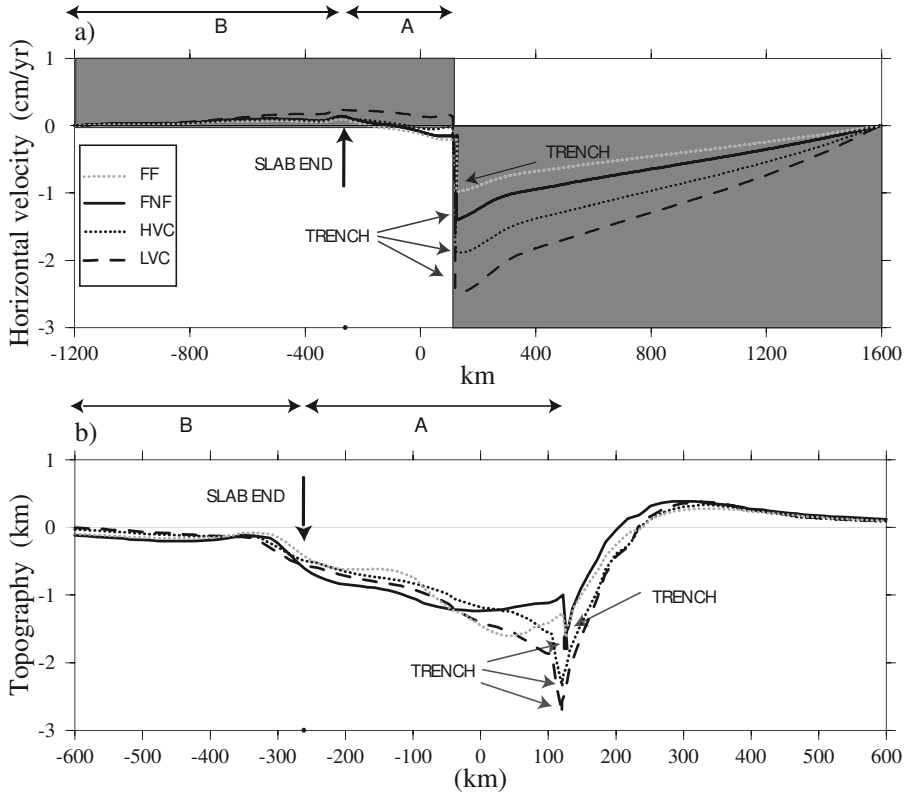


Figure 7. Surface expressions for models with land-locked basin boundary conditions. (a) Horizontal velocity at the surface of the model for the entire domain: solid curve represents frictionless fault model (FNF), grey dotted fault model with friction (FF), black dashed low viscosity channel (LVC) model $\eta = 7 \times 10^{17}$, black dotted high viscosity channel (HVC) model $\eta = 10^{20}$. Velocities in the grey area are directed towards the trench. (b) Total vertical displacement at the surface of the model. The vertical arrow indicates the vertically projected tip of the slab. The overriding plate is divided in region A and region B.

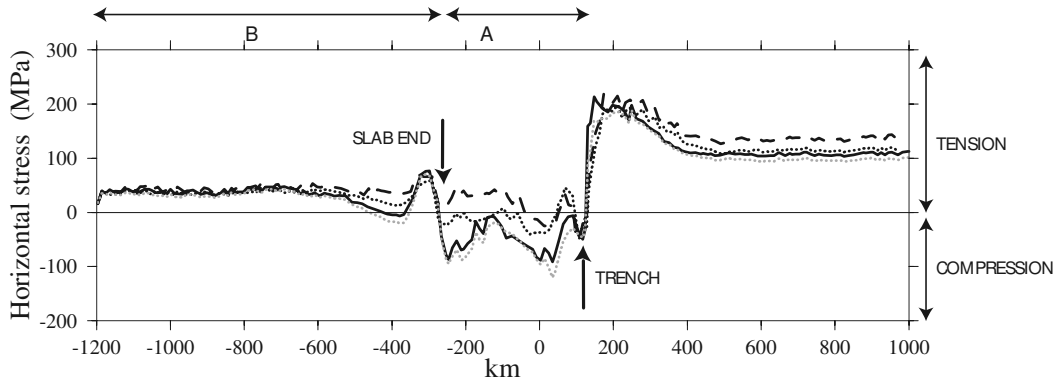


Figure 8. Horizontal stress at the free surface of the land-locked subduction models for the entire domain. Compression is negative. Solid line represents frictionless fault model (FNF), grey dotted line fault model with friction (FF), black dashed line low viscosity model (LVC), black dotted line high line viscosity model (HVC). The vertical arrows indicate the vertically projected tip of the slab and of the plate contact location. The upper plate is divided into region A and region B.

3.2.2 Frictional fault subduction zone model (FF)

In our next model we impose a uniform frictional shear stress of 20 MPa on the fault. The increased coupling results in a reduction of the relative velocity across the subduction zone (Fig. 7a, grey dotted line). The region of the overriding plate immediately close to trench subsides more strongly than in the FNF model, except for the region close to the plate contact (Fig. 7b, grey dotted line). The trench has deepened by 1.5 km. Relative to the FNF model, velocities are reduced.

The grey dotted curve in Fig. 8 shows the horizontal stress at the surface. The stress at the surface, is similar to the one of the FNF model, with compression in region A of the overriding plate. Relative to the FNF model, the overriding plate shows significantly stronger horizontal compression close to the plate contact. Similar to the FNF model, the surface oceanic plate is in horizontal tension.

3.2.3 Low viscosity subduction channel model (LVC)

As in the previous set of models we represent the subduction zone by a LVC ($\eta = 7 \times 10^{17}$ Pa s). The convergence velocity is higher by approximately 1 cm yr^{-1} than in the FNF model (Fig. 7a, dashed curve). In the overriding plate the velocity increases moving towards the trench with a maximum velocity in the area from 260 km to the

© 2006 The Authors, *GJI*, **171,** 435–450
Journal compilation © 2007 RAS

Downloaded from https://academic.oup.com/gji/article/171/1/435/2126031 by guest on 21 July 2021

plate contact (region A) of about 3 mm yr^{-1}. Subsidence is less than in the FNF model, except for the region close to the plate contact (Fig. 7b). The trench has deepened to less than 3 km, and is wider.

Stresses in the LVC model are generally different from the FNF and FF models in the overriding plate, in that weak horizontal tension prevails for nearly the entire overriding plate (Fig. 8, black dashed line regions A and B). Horizontal tensile stresses dominate in the surface oceanic plate with higher stress in the far field region than in the FNF and FF models.

3.2.4 High viscosity subduction channel model (HVC)

The Newtonian viscosity of the subduction channel in this model is 1×10^{20} Pa s. The overall response of this model is similar to the LVC model. The velocity of the subducting plate is less than in the LVC but higher than in the FNF and FF models (Fig. 7a, black dotted line). The most relevant change occurs in the horizontal stress in the overriding plate (Fig. 8, black dotted line region A), which is slightly compressive rather than tensile as in the LVC. Still, however, stress levels are low in comparison to the FNF and FF.

4 MODEL ANALYSIS

Comparing FNF, FF, LVC and HVC models for free subduction boundary conditions, we notice that the velocity in region A of the overriding plate is oriented in the same direction as in the subducting plate for all models. For the FNF model the magnitude of this velocity is higher than for all the other models. In the land-locked basin FNF model, the upper plate moves away from the trench, while in the LVC model the displacement direction is towards the trench. The FF and HVC models have an intermediate behaviour. When the overriding plate moves in the same direction as the subducting plate, a compressional regime develops in region A (e.g. Fig. 6). On the other hand, when the velocity is directed towards the plate contact, in the LVC land-locked basin setting, the regime in region A becomes tensional. This was also found by Heuret & Lallemand (2005). The fact that they fix the subduction hinge with respect to the upper plate edge does not change the meaning of their result. Our results indicate that the different velocity distributions, arising from different states of the plate contact, cause different stresses in FNF, FF, LVC and HVC. The question is why the velocity changes from one model to the other. In the setup of our experiments, the negative buoyancy of the subducted lithosphere with respect to the surrounding mantle is the primary driving force. This holds for all models. The secondary forces which play a role are the suction force, which acts at the plate interface and makes the plates interdependent (Bott *et al.* 1989; Whittaker *et al.* 1992), the force due to the bending of the lithosphere and frictional force in the models where friction is present (Fig. 9). These forces result in a state of stress in the lithosphere, which we characterize by the Response Force that we define as the difference between horizontal and vertical stress integrated with depth through the lithosphere. We calculate it at the left edge of the continental plate. The boundary conditions, applied at this edge (locked: zero horizontal displacement), do not affect the overall response of the model because they are far enough from the trench. This is proven by the fact that tension develops in the far field of the plate even though compression dominates in region A (e.g. Fig. 8). Now we consider just the two end members of our models, the FNF model and the LVC models. LVC is characterized by a stronger Response Force than the FNF model. The force magnitude increases from 2.2×10^{12} N m^{-1} in the FNF to 2.9×10^{12} N m^{-1} for LVC, respectively.

In the FNF model, the suction force is intrinsic in the fault description, since the normal stress and velocity are continuous at the fault and the two plates are fully coupled in that direction. The normal components of the forces, which act at the fault are transmitted from one plate to the other. The Response Force is the result of such normal continuity. When the fault is frictional (FF model) the overall response of the model is the same. The presence of friction develops compressive stresses along the plate contact and a compressive forearc region; clearly, the speed of subduction is reduced.

In the LVC model—and in general in any channel model (also in HVC model)—the nature of the Response Force is different. The channel, with its weak material, reduces the transmission of stresses between the plates, for example, the bending stress. Moreover, the low coupling between the plates increases the net downward force acting on the subducting plate. Shemenda (1993) showed that the interplate pressure is inversely proportional to the slab pull. As a consequence, the increase of slab pull decreases such a pressure.

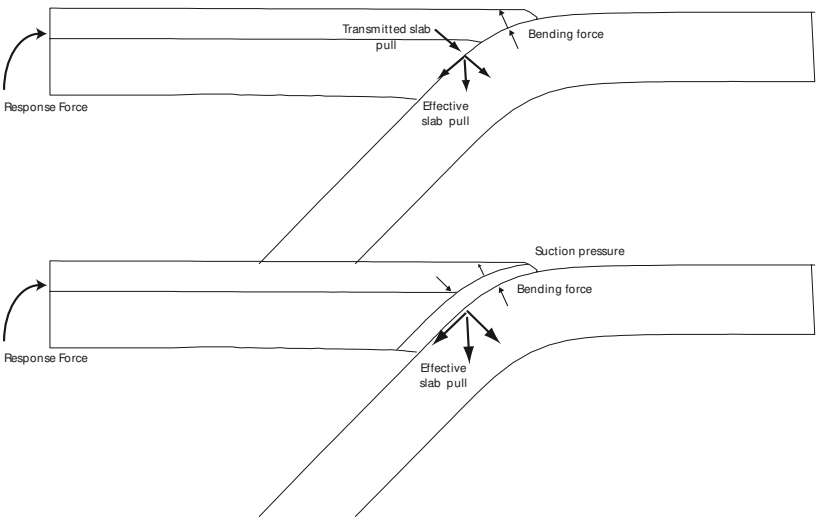


Figure 9. Top. Schematic sketch of forces acting at the fault, with the traction felt by the overriding plate as response to the bending stress and the traction due to the normal component of the gravitational force. The arrows represent the forces that are equal at both sides of the fault. Bottom. Forces acting in the channel model. The tractions are less transmitted, the net slab pull acting on the subducting plate is more in the FNF model. On the left-hand side it is indicated where the Response Force is measured.

Downloaded from https://academic.oup.com/gji/article/171/1/435/2126031 by guest on 21 July 2021

Shemenda (1993) proved that a low interplate pressure reduces compression of the overriding plate or it produces extension. In Fig. 9 the main forces in the process are summarized.

Several aspects in the dynamic response of the models are worth noticing. First, in the free subduction LVC and HVC the velocity magnitude of the overriding plate is reduced relative to the FNF and FF models. In the FNF and FF models the forces are fully transmitted at the plate contact pushing the overriding plate towards the left. In the LVC and HVC the lower transmission of forces through the plate interface reduces such a push and as a consequence the compressive regime. Second, the velocity of the slab is faster in the LVC and HVC than in the FNF and FF models. Third, the velocity field in the slab is more slab parallel in the LVC and HVC models than in the FNF and FF models. In the land-locked basin LVC subduction model the roll-back of the slab, in addition to the stronger net slab pull, makes the overriding plate advance. A higher channel viscosity (HVC) reduces the trench-ward velocity of the overriding plate and increases the compressive stress in the forearc region. This is a direct consequence of the increase of friction and transmission of stress from one plate to the other, and of the increase of the interplate pressure.

As the subduction velocity is generally lower in the FNF model than in the LVC model, it is understandable that the magnitude of the excited Response Force is less. To show that the plate boundary type, rather than the subduction velocity, determines the stress field and the amount of subsidence of the overriding plate, we consider two new models involving a FNF and a LVC type of plate contact. Now, the subducting plate is driven by velocity boundary conditions which are applied on the slab and on the right boundary of the oceanic lithosphere. The continental plate is again fixed on the left-end side. In Fig. 10(a), the horizontal velocity at the surface of the model is displayed. The FNF model (solid line) is characterized by a retreating upper plate, while in the LVC model

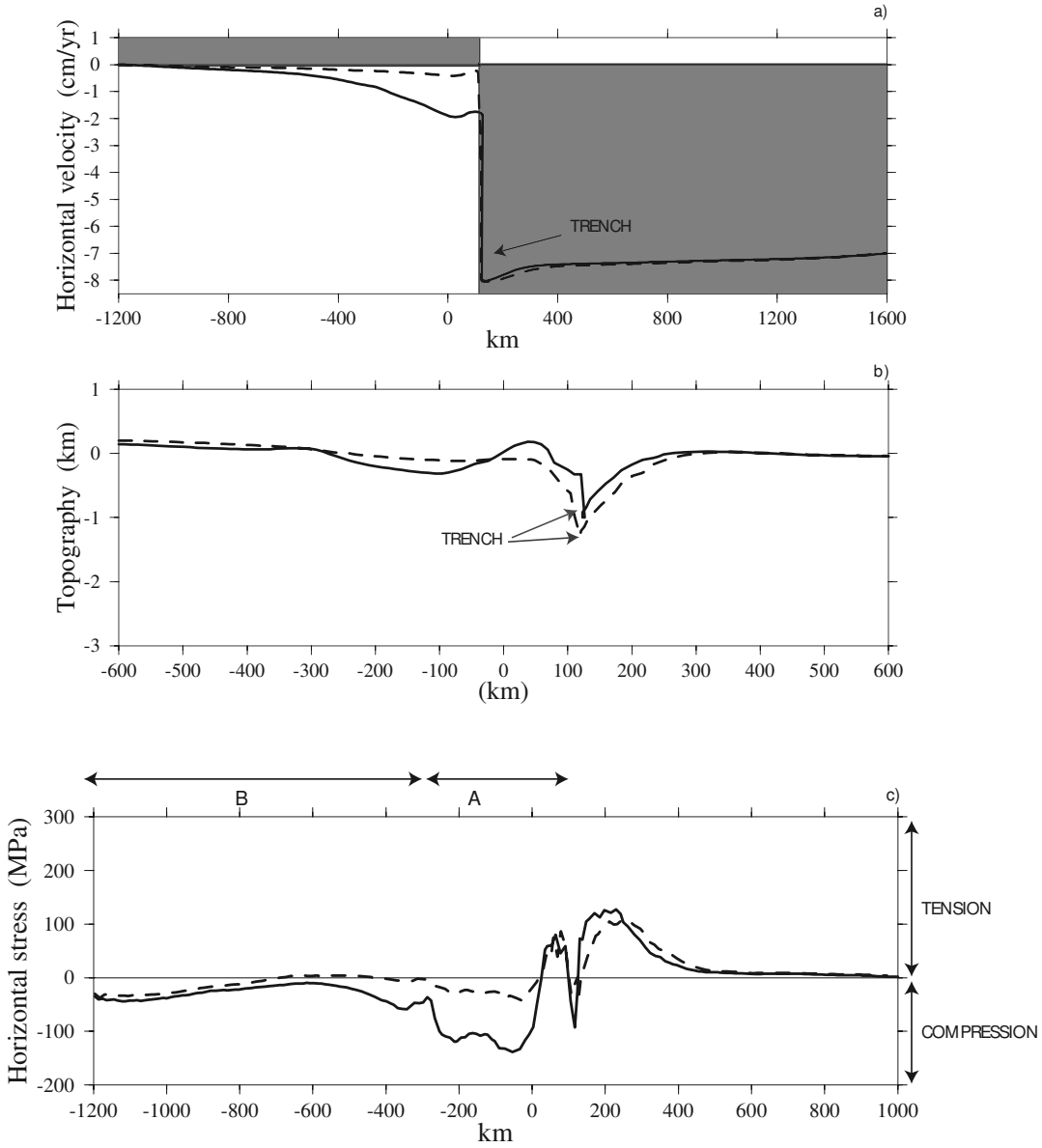


Figure 10. Surface expression of velocity driven models at the free surface. Solid curve represents the frictionless fault model (FNF), the dashed curve the low viscosity channel model (LVC). (a) Horizontal velocities. Velocity in the grey area are directed towards the trench. (b) Total vertical displacement. The deepest point is the trench location. (c) Horizontal stress. Compression is negative.

© 2006 The Authors, *GJI*, **171,** 435–450
Journal compilation © 2007 RAS

Downloaded from https://academic.oup.com/gji/article/171/1/435/2126031 by guest on 21 July 2021

(dashed line) the plate is close to stationary. Fig. 10(b) shows the total vertical displacement. Subsidence is stronger on the overriding plate of the FNF model (solid line) than the LVC model (dashed curve) except for the region immediately close to the plate contact. At the bottom, the horizontal stresses are displayed: in region B of the upper plate both models show the same amount of compression; in part of region A of the FNF model compression is, whereas in the LVC model the compressive stresses are reduced by about 70 per cent.

In the FNF model, the only force perpendicular to the fault is caused by the bending of the slab, the stresses generated are completely transmitted to the overriding plate at the shallow part of the fault, causing the retreat of the upper plate. In the channel models, the reduced transmission of the bending stresses and of the slab pull result in more subsidence close to the plate contact, less retreat, less down-welling above the slab end and lower compressive stress. In the land-locked basin FNF model the compression in the overriding plate above the dipping slab outweighs the tension produced by slab roll-back so that a net compressive stress persists into the backarc region. The horizontal compressive stresses and the down-welling above the slab end are due to the fact that the overriding plate retreats. This explains why in FNF the overriding plate experiences upwelling in the region immediately close to the plate contact.

The land-locked basin LVC produces tension in region A, even though the amount of slab roll-back is less than in the FNF model (see the online Supplementary Material section Figs 2(a) and (c). In the free subduction setup the compressive regime is reduced relative to the FNF model as well as the down-welling.

On the basis of our numerical models, we conclude that the nature of the plate contact is a primary controlling factor in developing or not of backarc extension. The plate contact type controls the dynamic response of the upper plate, drives the displacement of the overriding plate and as a consequence the stress distribution. Comparing fault and channel models, we conclude that the subduction channel reduces the compression in the region of the overriding plate above the slab, in a convergent tectonic setting (e.g. free subduction and kinematically driven model). The subduction channel—if the rheology is weak enough (e.g. LVC)—produces tension in a land-locked basin setting. The fault model, however, results in a compressive regime, even with a larger amount of slab roll-back than in the channel model.

Many numerical studies have been carried out subduction process behaviour (e.g. van Hunen *et al.* 2000; Funiciello *et al.* 2003; Kincaid & Hall 2003; Hampel & Pfiffner 2006). In this section we compare our models with the ones that are more closely related to our study, and we investigate, in a similar set-up, the same kind of observed parameters. Whittaker *et al.* (1992) used both locked and unlocked fault plate contact. The model with a locked fault showed results similar to our frictional model: compression was developed in the overriding plate close to the trench and in the backarc region and the displacement displayed a broad down flexure at the surface above the slab. However, their unlocked model showed a different behaviour compared to our FNF model. They obtained tension in the overriding plate. We can trace two reasons. First the fault extends until the end of the slab (in our model the fault is just at the contact between the two plates); in this way less asthenosphere was dragged down, reducing the down-welling of the lithosphere. Second, the continental crust in their model was 400 kg m^{-3} lighter than the surrounding mantle, which resulted in tensile stress regime of the overriding plate. So, their continental crust contributed to the forcing.

Comparing our model with the model of Giunchi *et al.* (1996) in which the fault is located just along the plate contact (their Locked model), we find both similarities and differences. The horizontal velocities showed the same pattern: the overriding plate retreated in the region close to the plate contact, but the magnitude in the subducting plate was lower in their model. This is due to the boundary conditions that in our models are farther from the trench. The vertical velocity showed a pattern comparable to our vertical displacement. The total velocity distribution displayed similar features, with the overriding plate moving in vertical direction and a strong near horizontal flow in the mantle. Their stress distribution, with the overriding plate in compression and very small stresses close to the plate contact, is also comparable to ours. It is interesting to notice that as soon as they unlocked the fault down to the end of the slab, the overriding plate started to move towards the trench and the horizontal compressive stresses became negligible. Overriding plate tension in their model was caused by two factors; the zero friction along the entire slab top surface reduced the drag of the asthenosphere and of the above lithosphere, and the dip angle which is 70° in their model. This steep angle leads to a stronger suction force causing tension in the overriding plate. Zhong *et al.* (1998) found that, when a curved fault of 100 km depth and a dip angle of about 45° were introduced at the contact between overriding and subducting plate, the upper plate was affected by horizontal compression. This is in agreement with our FNF results.

5 DISCUSSION

In previous studies, different hypotheses have been proposed in order to explain what governs the stress regime in the upper plate. Some classical theories are: (1) backarc extension driven by roll-back caused by negative buoyancy of the slab which is a function of the age of the slab (Elsasser 1971; Molnar & Atwater 1978; England & Wortel 1980; Faccenna *et al.* 2001; Hall *et al.* 2003; Schellart *et al.* 2003); (2) backarc extension driven by absolute motion of the overriding plate (Chase 1978; Scholz & Campos 1995). Observed evidence supports neither hypothesis completely (Lallemand *et al.* 2005; Sdrolias & Dietmar Muller 2006). For the investigated tectonic settings, our models show that the velocity of the upper plate and the stress distribution of part of the upper plate are driven by the dynamic response of the subduction zone to the combination of suction force, transmission of bending stress and gravity. The dynamic response was measured at the edge of the upper plate, resulting in what we called Response Force. The LVC increases the magnitude of Response Force and produces tension even with a small amount of slab roll-back. As a consequence, although roll-back is required as a underling mechanical process, there is not a one-to-one relationship between roll-back and stress regime. The type of plate contact plays a decisive role in controlling backarc state of stress. These findings give a new insight in the mechanisms controlling the stress regime of the overriding plate.

This study has taken a step in the direction of defining the relations between plate contact type and stress regime of the overriding plate. However, there are some open problems related to the subduction channel. As pointed out by Eberhart-Phillips & Martin (1999), large thrusting events have been recorded near the plate interface where LVC are present, for example, subduction of the Hikurangi Plateau. The problem arising from the presence of the LVC, that is characterized by a weak rheology, is how to explain these events. We think that, during evolution of a subduction zone, the interface can change from a plate contact like channel to a fault and vice versa. A very critical factor, as pointed out by Cloos & Shreve (1988) is the sediment supply; if the channel is thick, or has a very low viscosity, the average shear stress is relatively low. Then thrust earthquakes

Downloaded from https://academic.oup.com/gji/article/171/1/435/2126031 by guest on 21 July 2021

are more likely when the channel is so thin that it mechanically acts like a fault. Another possibility is that asperities in the channel, such a seamounts, may be sites of concentrated seismic activity (Ruff & Kanamori 1983).

One limitation of our model is that the slab hangs from the top implying that the most of the slab weight is supported by the plates. We expect to obtain different results using a slab that is largely supported from below, that is, a slab reaching the 670 km discontinuity.

In this study, the numerical experiments are limited to free subduction and land-locked basin subduction, in both cases the overriding plate is locked. This derives from our starting point only to consider the cases where the forcing occurs within our model domain. As a consequence, however, our models do not encompass the entire range of tectonic settings; for instance, we did not consider the case of an overriding plate that is actively driven towards the trench by forces outside the model domain. Surely, our conclusions about the stress regime in the overriding plate will be affected by such boundary push or pull. For instance, if the overriding plate is actively driven towards the trench, it may mask the signature of backarc extension. We did not investigate the influence of the slab age; this is based on the fact that the age-dependent slab pull force contributes either slightly or not at all to slab roll-back that could explain backarc extension (Lallemand *et al.* 2005). We need to point out that in our dynamic models we neglect domain-internal ridge push in order to isolate the subduction effect. This force is present in most of the edge plates and could influence the stress distribution within the plates. In the kinematically driven model, where we imposed ridge push through velocity boundary conditions, compression affects the entire overriding plate for both FNF and LVC. However, the amount of compression is strongly reduced by the presence of the LVC. Thus, we argue that, even in a convergent tectonic setting, the different response due to presence of the LVC is well recognizable.

The LVW above the slab reduces the link between the overriding plate and the sinking slab. This feature makes it difficult to distinguish, in the surface response, between the contribution of such weak region and the flow generated by the eddies in the mantle. However, this does not affect our conclusions, in which we want to establish the differences due to the two types of plate contact using the same type of tectonic setting and forces.

Another limitation is that we did not investigate alternate subduction geometries; the influence of slab dip or different radius of curvature of the plate contact. We speculate that these parameters do not change our general conclusions, because, even though the results may be affected by them—for example, the dip angle is correlated to the stress regime of the overriding plate—the response of the subduction process is intrinsically related with the type of plate boundary. Thus, comparing FNF and LVC for different kinds of geometry or rheology, we will anyway observe different signatures. This is due to the fact that FNF and LVC represent different physical states of the subduction plate contact.

6 CONCLUSIONS

Based on a consistent comparison of fault and channel numerical models, we conclude that the nature of the plate contact is one of the controlling factors in developing or not of backarc extension. Our results indicate that the different dynamic response in the overriding and subducting plate, arising from the state of the plate contact, causes different velocities and stresses in fault models and channel models:

(i) if the subducting plate is free to move in horizontal direction (i.e. free subduction), the fault models are characterized by: (1) subsidence of the overriding plate above the slab; (2) imperfect plate like behaviour of the subducting plate; (3) motion of the overriding plate away from the trench; (4) compression of the backarc region ranging between the trench and the vertically projected tip of the slab. Specifically, when friction is present at the fault, subduction velocities are reduced, and subsidence of the overriding plate region close to the plate contact is more developed.

Relative to the fault models, the channel models are characterized by: (1) less vertical deformation above the slab end, therefore the subsidence is reduced; (2) more subsidence close to the plate contact; (3) faster subduction and a more plate like motion; (4) less motion of the overriding plate away from the trench, due to the combination of suction force and the low transmission of stress between the plates; (5) lower compressive stresses in the overriding plate region ranging between the trench and the vertically projected tip of the slab;

(ii) If no relative motion between the far field of the two plates is allowed (i.e. land-locked basin setting), the fault models are characterized by: (1) subsidence of the overriding plate; (2) motion of the overriding plate away from the trench; (3) backarc compression of the upper plate in the region between the trench and the vertical projected tip of the slab. Slab roll-back does not produce tension in this region, but tension is generated in the far field region of the overriding plate.

Again relative to the fault models, the channel models are characterized by: (1) reduced subsidence of the upper plate above the slab end; (2) more subsidence close to the plate contact; (3) faster subduction velocity; (4) upper plate moving towards the trench; (5) tension in the entire upper plate for LVC model and lower compression in the region of the overriding plate above the slab for HVC model. This shows that even though slab roll-back is less developed than in the fault model, tension may result in the entire overriding plate of our model

We conclude that, the type of plate contact plays a decisive role in controlling the backarc state of stress. To obtain backarc extension, roll-back is required as an underlying geodynamic process, but it is not always a sufficient condition.

ACKNOWLEDGMENTS

Partial support for RDF and computational resources for this work were provided by the Netherlands Research Center for Integrated Solid Earth Science (ISES 3.2.5; High End Scientific Computation Resources). The authors would like to thank C. Faccenna and an anonymous reviewer for the helpful suggestions which helped to improve the manuscript.

REFERENCES

Abers, G.A., 2005. Seismic low-velocity layer at the top of subducting slabs: observations, predictions, and systematics, *Phys. Earth Planet. Inter.*, **149,** 7–29.

Baley, S., Gropp, W. D., McInnes, L. C.& Smith, B. F., 2002. Petsc users manual technical report ANL-95/11-Revision 2.1.2., Angomme National Laboratory.

Beaumont, C. & Ellis, S., 1999. Dynamics of sediment subduction-accretion at convergent margins: short-term modes, long-term deformation, and tectonic implications, *J. geophys. Res.,* **104**(B8), 17 573–17 601.

Billen, I.B. & Gurnis, M., 2001. A low viscosity wedge in subduction zones, *Earth Planet. Sci. Lett.,* **193,** 227–236.

Downloaded from https://academic.oup.com/gji/article/171/1/435/2126031 by guest on 21 July 2021

Bott, M.H.P., Waghorn, G.D. & Whittaker, A., 1989. Plate boundary forces at subduction zones and trench-arc compression, *Tectonophysics,* **170,** 1–15.

Brooks, A.N. & Hughes, T.J.R., 1982. Streamline upwind/Petrov-Galerkin formulations for convection dominated flows with particular emphasis on the incompressible Navier-Stokes equations, *Comput. Methods Appl. Mech. Eng.,* **32,** 199–259.

Buiter, S., Govers, R. & Wortel, M.J.R., 2001. A modelling study of vertical surface displacements at convergent plate margins, *Geophys. J. Int.,* **147,** 415–427.

Byerlee, J., 1978. Friction of rocks, *Pageoph,* **116,** 615–626.

Chase, C.G., 1978. Extension behind island arcs and motions relative to hotspots, *J. geophys. Res.,* **83,** 5380–5387.

Chopin, C., 2001. Coesite and pure pyrote in high-grade blueshists of the western Alps: a first record and some consequences, *Contribution to Mineralogy and Petrology,* **86,** 107–118.

Cloos, M. & Shreve, R.L., 1988. Subduction channel model of prism accretion, melange formation, sediment subduction, and subduction erosion at convergent plate margins: 2. Implications and discussion, *Pageoph.,* **128,** 501–545.

Davies, G.F. & Brune, J.N., 1971. Regional and global fault slip rates from seismicity, *Nature,* **229,** 101–107.

Eberhart-Phillips, D. & Martin, R., 1999. Plate interface properties in the northeast Hikurangi subduction zone, New Zeland, from converted seismic waves, *Geophys. Res. Lett.,* **26,** 2565–2568.

Elsasser, W.M., 1971. Seafloor spreading as thermal convection, *J. geophys. Res.,* **76,** 1101–1112.

England, P. & Wortel, R., 1980. Some consequences of the subduction of young slabs, *Earth Planet. Sci. Lett.,* **47,** 403–415.

England, P.C. & Holland, T.J.B., 1979. Archimeded and Tauren eclogites: the role of buoyancy in the preservation of exotic eclogite blocks, *Earth Planet. Sci. Lett.,* **44,** 287–294.

Faccenna, C., Funiciello, F., Giardini, D. & Lucente, P., 2001. Episodic back-arc extension during restricted mantle convection in the central Mediterrean, *Earth Planet. Sci. Lett.,* **187,** 105–116.

Freed, A.M. & Burgmann, R., 2004. Evidence of power-law flow in the Mojave desert mantle, *Nature,* **430,** 548–551.

Funiciello, F., Morra, G., Regenauer-Lieb, K. & Giardini, D., 2003. Dynamics of retreating slab: 1. insights from two-dimensional numerical experiments, *J. geophys. Res.,* **108**(B4), doi:10.1029/2001JB000898.

Gerya, T.V., Stockhert, B. & Perchuck, A.L., 2002. Exhumation of high-pressure metamorphic rocks in a subduction channel: a numerical simulation, *Tectonics,* **21**(6), 227–236.

Giunchi, C., Sabadini, R., Boschi, E. & Gasperini, P., 1996. Dynamic models of subduction: geophysical and geological evidence in the Tyrrhenian Sea, *Geophy. J. Int,* **126,** 555–578.

Govers, R. & Wortel, M.J.R., 1993. Initiation of asymmetric extension in continental lithosphere, *Tectonophys.,* **223,** 75–96.

Govers, R. & Wortel, M.J.R., 2005. Lithosphere tearing at STEP faults: Response to edges of subduction zones, *Earth planet. Sci. Lett.,* **236,** 505–523.

Hall, R., Gurnis, M., Sdrolias, M., Lavier, L.L. & Muller, R.D., 2003. Catastrophic initiation of subduction following forced convergence across fracture zones, *Earth planet. Sci. Lett.,* **212,** 15–30.

Hampel, A. & Pfiffner, A., 2006. Relative importance of trenchward upper plate motion and friction along the plate interface for the topographic evolution of subduction-related mountain belts, *Geol. Soc. London, Spec. Publ.,* **253,** 105–115.

Heuret, A. & Lallemand, S., 2005. Plate motions, slab dynamics and back-arc deformation, *Phys. Earth Planet. Inter.,* **149,** 31–52.

Jacoby, W.R. & Schmeling, H., 1982. On the effects of the lithosphere on mantle convection and evolution, *Phys. Earth Planet. Inter.,* **29,** 305–319.

Kanamori, H., 1977. The energy realized in great earthquakes, *J. Geophys. Res.,* **82,** 2981–2987.

Kapitzke, U., 1979. Finite element convection models: comparison of shallow and deep mantle convection, and temperatures in the mantle, *J. geophys. Res.,* **46,** 97–121.

Karato, S. & Wu, P., 1993. Rheology of the upper mantle: a synthesis, *Science,* **260,** 771–778.

Kincaid, C. & Hall, P.S., 2003. Role of back arc spreading in circulation and melting at subduction zones, *J. geophys. Res.,* **108**(B5), 1025–1928.

Kohlsteldt, D.L. & Zimmerman, M.E., 1996. Rheology of partially molten mantle rocks, *Annu. Rev. Earth Planet. Sci.,* **24,** 41–62.

Lallemand, S., Heuret, A. & Boutelier, D., 2005. On the relationships between slab dip, back-arc stress, upper plate absolute motion, and crustal nature in subduction zones, *Geochem. Geophys. Geosyst,* doi: 10.1029/2005GC000917.

Le Pichon, X., 1982. Land-locked oceanic basins and continental collision: the Eastern Mediterranean as a case example, in *In Mountain Building Processes*, pp. 201–211, ed. Hsu, K., Academic Press London, UK.

Melosh, H.J. & Raefsky, A., 1983. A realistic response of the earth to dip slip earthquakes, *J. Geophys. Res.,* **88,** 515–526.

Mitrovica, J.X. & Forte, A.M., 1997. Radial profile of mantle viscosity: results from the joint inversion of convection and postglacial rebound observables, *J. geophys. Res.,* **102,** 2751–2769.

Mizukami, A., 1985. An implementation of streamline upwind, Petrov-Galerkin method for triangular elements, *Comp. Meth. Appl. Mech. Eng,* **49,** 357–364.

Molnar, P. & Atwater, T., 1978. Interact spreading and Cordillera tectonics as alternatives related to the age of the subducted oceanic lithosphere, *Earth Planet. Sci. Lett.,* **41,** 330–340.

Oncken, O., Sobolev, S. & Sitller, M., 2003. Seismic imaging of a convergent continental margin and plateau in the central Andes (Andean Continental Research Project 1996 (ANCORP' 96)), *J. Geoph. Res.,* **108**(B7), Art. No. 2328.

Patankar, S.V., 1980. Computational methods in mechanics and thermal sciences, in *Numerical Heat Transfer and Fluid Flow*, Hemisphere Publishing Corporation, New York.

Renner, J., Stockhert, B., Zerbian, A.K.R. & Rummel, F., 2001. An experimental study into the rheology of synthetic polycrystalline coesite aggregates, *J. Geophys. Res.,* **106,** 19 411–19 429.

Ruff, L.J. & Kanamori, H., 1983. Seismic coupling and uncoupling at subduction zones, *Tectonophysics,* **99,** 99–117.

Schellart, W.P., Jessel, M.N. & Lister, G.S., 2003. Asymmetric deformation in the back arc region of the Kuril Arc, northwest Pacific: new insights from numerical modeling, *Tectonics,* **22**(5), 1047, doi:10.1029/2002TC001473.

Schmeling, H. & Jacoby, W.R., 1981. On modelling the lithosphere in mantle convection with non linear rheology, *J. geophys. Res.,* **50,** 89–100.

Scholz, C.H. & Campos, J., 1995. On the mechanism of the seismic decoupling and back-arc spreading at subduction zone, *J. geophys. Res.,* **100,** 22 103–11 115.

Sdrolias, M. & Dietmar Muller, R., 2006. Controls on back-arc basin formation, *Geochem. Geophys. Geosyst,* **7**(4), doi:10129/2005GC001090.

Segal, A., 1993. Finite element methods for advection-diffusion equations, in *Numerical Methods for Advection Diffusion Problems, Series in Notes on Numerical Fluid Mechanics*, pp. 195–214, eds Vreugdenhil, C.B. & Koren, B., Vieweg, Braunschweig, Wiesbaden.

Shemenda, A.I., 1993. Subduction of the lithosphere and Back arc dynamics: insights from physical modeling, *J. geophys. Res.,* **98**(B9), 16 167–16 185.

Shreve, R.L. & Cloos, M., 1986. Dynamics of sediment subduction, melange formation, and prism accretion, *J. Geophys. Res.,* **91**(B10), 10 299–10 245.

Smith, D.C., 1984. Coesite in clinopyroxene in the Caledonides and its implications for geodynamics, *Nature,* **310,** 641–644.

Stockhert, B., 2002. Stress and deformation in subduction zones—insight from record of exhumed high pressure metamorphic rocks, *Geol. Soc. Spec. Publ.,* **200,** 255–274.

Tackley, P.J., 2000. Mantle convection and plate tectonics: toward an integrated physical and chemical theory, *Science,* **288,** 2002–2007.

Tichelaar, B.W. & Ruff, L.J., 1993. Mantle convection and plate tectonics: toward an integrated physical and chemical theory, *J. Geophys. Res.,* **98**(B2), 2017–2037.

Tsuru, T., Park, J.O., Miura, S., Kodaira, Y. & Hayashi, T., 2002. Along-arc structural variation of the plate boundary at the Japan Trench margin: implication of intraplet coupling, *J. geophys. Res.,* **107**(B12), Art. No 2357.

van de Zedde, D.M.A. & Wortel, M.J.R., 2001. Shallow slab detachment as

Downloaded from https://academic.oup.com/gji/article/171/1/435/2126031 by guest on 21 July 2021

a transient source of heat at midlithospheric depths, *Geochem. Geophys. Geosyst,* **6**(20), 868–882.

van Hunen, J., van den Berg, A. & Vlaar, N.J., 2000. Subduction erosion and basal friction along the sediment-starved convergent margin off Antofagasta, Chile, *Earth Planet. Sci. Lett.,* **182,** 157–169.

van Thienen, P., van den Berg, A.P., de Smet, J.H., van Hunen, J. & Drury, M.R., 2003. Interaction between small-scale mantle diapirs and continental root, *Geochem. Geophys. Geosyst.,* **4**(2), 8301, doi:10.1029/2002GC000338.

Whittaker, A., Bott, M.H.P. & Waghorn, G.D., 1992. Stress and plate boundary force associated with subduction, *J. Geophys. Res.,* **97**(B8), 11 933–11 944.

Zhong, S. & Gurnis, M., 1994a. Controls on trench topography from dynamic models, *J. Geophys. Res.,* **99**(B8), 15 683–15 695.

Zhong, S. & Gurnis, M., 1994b. Role of plates and temperature-dependent viscosity in phase change dynamics, *J. Geophys. Res.,* **99**(B8), 15 903–15 917.

Zhong, S., Gurnis, M. & Moresi, L., 1998. Role of faults, nonlinear rheology, and viscosity structure in generating plates from instantaneous mantle flow models, *J. Geophys. Res.,* **103**(B7), 15 255–15 268.

APPENDIX A: FINITE ELEMENT EQUATION FOR DIFFUSION-ADVECTION EQUATION

The partial differential equation (PDE) for the convection-diffusion problem including sources is:

$$\nabla\times(k\nabla T) + g - \rho C_p \mathbf{v}\times\nabla T = 0, \tag{A1}$$

where k denotes the diffusivity, T denotes the temperature, g denotes the heat production, ρ denotes the density, C_p denotes the specific heat at constant pressure, $\mathbf{v}$ denotes the given velocity vector.

We rewrite the equation above through the finite element formulation in the Standard Galerkin Approach (SGA). The SGA is based on the weak formulation of eq. (A1). This formulation arises by multiplication of the differential equation by the test function, which in our case is the shape function and afterwards integration over the domain. The eq. (A1) becomes:

$$\int_{V^{(e)}} N_i \left[\frac{\partial}{\partial x}\left(k_x\frac{\partial T^{(e)}}{\partial x}\right) + \frac{\partial}{\partial y}\left(k_y\frac{\partial T^{(e)}}{\partial y}\right) + \frac{\partial}{\partial z}\left(k_z\frac{\partial T^{(e)}}{\partial z}\right)\right] \mathrm{d}V \tag{A2}$$

$$+\int_{V^{(e)}} N_i g\, dV - \int_{V^{(e)}} \rho C_p N_i \times\left[v_x^{(e)}\frac{\partial T^{(e)}}{\partial x} + v_y^{(e)}\frac{\partial T^{(e)}}{\partial y} + v_z^{(e)}\frac{\partial T^{(e)}}{\partial z}\right]\mathrm{d}V = 0, \tag{A3}$$

where $V^{(e)}$ is the element volume, and $T^{(e)} = \sum_{j=1}^{NEN} N_j T_j$ is temperature in the element, NEN is the nodes element numbers. N_j are shape functions prescribed in terms of independent variables and all or some of the parameters T_j are unknown. Element velocities derive from the same interpolation function, that is, $v_x^{(e)} = \sum_{j=1}^{NEN} N_j v_j^x$ and so on, where $\hat{\mathbf{v}}_j = (v_j^x, v_j^y, v_j^z)$ is the velocity vector at node j. In a concise form eq. (A2) is:

$$\mathbf{KT} = \mathbf{P}, \tag{A4}$$

where $\mathbf{K}$ is the stiffness matrix and $\mathbf{P}$ is the right-hand side vector. Following partial integration (i.e. using Gauss' divergence theorem) and ignoring surface integral—surface integral of neighboring elements are assumed to cancel after assembly—we obtain the expression for the stiffness matrix:

$$K_{ij}^{(e)} = \int_{V^{(e)}}\left(k_x\frac{\partial N_i}{\partial x}\frac{\partial N_j}{\partial x} + k_y\frac{\partial N_i}{\partial y}\frac{\partial N_j}{\partial y} + k_z\frac{\partial N_i}{\partial z}\frac{\partial N_j}{\partial z}\right)\mathrm{d}V + \int_{V^{(e)}}\rho C_p N_i\left(v_x^{(e)}\frac{\partial N_j}{\partial x} + v_y^{(e)}\frac{\partial N_j}{\partial y} + v_z^{(e)}\frac{\partial N_j}{\partial z}\right)\mathrm{d}V. \tag{A5}$$

A1 Streamline upwind Petrov-Galerkin method

The above SGA behaves like a central difference scheme. For large Peclet numbers, central differences behave notoriously poor (e.g. Patankar 1980). In the finite difference and finite volume literature, upwind techniques have successfully been employed to remedy this. Segal (1993), based mostly on the work of Brooks & Hughes (1982), summarizes the streamline upwind Petrov-Galerkin (SUPG) method for finite elements. As in SGA, SUPG uses the weak formulation, with the difference that the weighting functions are chosen differently:

$$M = N + Q, \tag{A6}$$

where N is the classical shape function, and Q is a correction that takes care of the upwinding part. N is a continuous function while Q is allowed to be discontinuous over element boundaries. For this reason the Gauss divergence theorem can be applied just to N part.

A common choice for the function Q is inspired by the 1-D stationary convection–diffusion equation without source terms:

$$\rho C_p \mathbf{v}\times\nabla T = \nabla\times(\mathbf{k}\nabla T). \tag{A7}$$

The standard first order finite difference upwind scheme for the equation above may be considered as the central difference scheme corresponding to the equation

$$\rho C_p \mathbf{v}\times\nabla T = \nabla\times[(k+\hat{k})\nabla T], \tag{A8}$$

where $\hat{k}$ is called the artificial diffusion tensor. In the streamline-upwind method, In order to avoid inaccuracies, artificial diffusion acts only in the direction of the flow. To that end, $\hat{k}$ is parametrized as

$$\hat{k}_{ij} = \bar{k}\hat{v}_i\hat{v}_j \qquad \hat{v}_i \equiv \frac{v_i}{||v||} \qquad \hat{v}_j \equiv \frac{v_j}{||v||} \qquad ||v||^2 \equiv v_i v_i.$$

The value of $\bar{k}$ follows from summing the convective central difference term and the artificial diffusion term and assuming that this sum corresponds to the difference upwind scheme of the convective term.

The next step is to construct a function Q such that an artificial diffusion term is created, in order to do that is sufficient to choose the component Q_i equal to

$$Q_i \equiv \frac{\bar{k}}{\rho C_p ||v||^2}\hat{v}_m\frac{\partial N_i}{\partial x_m}. \tag{A9}$$

Classical, or pure, upwinding in more dimensions results in

$$Q_i = \bar{D}\,(v\times\nabla N_i) \qquad \bar{D} \equiv \frac{h_m|v_m|}{2||v||^2},$$

h_x, h_y and h_z are element sizes in the x, y and z-direction, respectively. However, pure upwind results in overly diffusive solutions. Therefore a optimizing contributions of (underdiffusive) central differences and (overdiffusive) upwind differences is used (Brooks & Hughes 1982). Introducing directional weighing functions ξ_x, ξ_y and ξ_z, Q_i is modified w.r.t. the above definition;

$$\bar{D} \equiv \frac{h_m|v_m|\xi_m}{2||v||^2}. \tag{A10}$$

Downloaded from https://academic.oup.com/gji/article/171/1/435/2126031 by guest on 21 July 2021

In G-TECTON the Mizukami scheme is used that is an extension of the above formulation for triangles (Mizukami 1985). Weighting functions are functions of directional Peclet numbers

$$(\xi_x, \xi_y, \xi_z) = \left[f\left(\frac{v_x h_x}{2\kappa}\right), f\left(\frac{v_y h_y}{2\kappa}\right), f\left(\frac{v_z h_z}{2\kappa}\right)\right], \tag{A11}$$

where κ is the thermal diffusivity. The following choices of $f(\alpha)$ are commonly proposed:

Classical upwind scheme $f(\alpha) = \text{sign}(\alpha)$
Optimal upwind scheme $f(\alpha) = \coth(\alpha) - 1/\alpha$

Double asymptotic approximation $f(\alpha) = \begin{cases} \alpha/3 & -3 \le \alpha \le 3 \\ \text{sign}(\alpha) & \alpha > 3 \end{cases}$

Critical approximation scheme $f(\alpha) = \begin{cases} -1 - 1/\alpha & \alpha \le -1 \\ 0 & -1 \le \alpha \le 1 \\ 1 - 1/\alpha & \alpha \ge 1 \end{cases}$

SUPG results in a modified stiffness matrix

$$K_{ij}^{(e)} = \int_{V^{(e)}} \left(k_x \frac{\partial N_i}{\partial x}\frac{\partial N_j}{\partial x} + k_y \frac{\partial N_i}{\partial y}\frac{\partial N_j}{\partial y} + k_z \frac{\partial N_i}{\partial z}\frac{\partial N_j}{\partial z}\right) \mathrm{d}V + \int_{V^{(e)}} \rho C_p (N_i + Q_i) \left(v_x^{(e)} \frac{\partial N_j}{\partial x} + v_y^{(e)} \frac{\partial N_j}{\partial y} + v_z^{(e)} \frac{\partial N_j}{\partial z}\right) \mathrm{d}V. \tag{A12}$$

The second term destroys the typical symmetry of the stiffness matrix, and necessitates us to use a different solver. Here we choose the generalized minimum residual method Krylov subspace method as implemented in the PETSc package (Balay et al. 2002; http://www-unix.mcs.anl.gov/petsc).

The resulting element load vector

$$P_i^{(e)} = \int_{V^{(e)}} g\,(N_i + Q_i)\,\mathrm{d}V - \int_{S^{(e)}} q_n N_i \mathrm{d}S \tag{A13}$$

Extensive testing of the implementation showed that it performs very well for incompressible flow fields. One particularly tough and successful test (more difficult than probably ever encountered in earth science applications) is the high Peclet number circular rotation test (Brooks & Hughes 1982).

SUPPLEMENTARY MATERIAL

The following supplementary material is available for this article:

Appendix S1. Complete results for the land-locked basin models.

This material is available as part of the online article from:

http://www.blackwell-synergy.com/doi/abs/10.1111/j.1365-246X.2006.03498.x

(this link will take you to the article abstract).

Please note: Blackwell Publishing are not responsible for the content or functionality of any supplementary materials supplied by the authors. Any queries (other than missing material) should be directed to the corresponding author for the article.

Downloaded from https://academic.oup.com/gji/article/171/1/435/2126031 by guest on 21 July 2021